Delft University of Technology

Magnetomechanical response of a steel monopile during impact pile driving
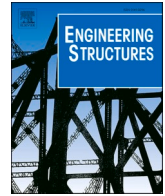
Meijers, P.C.; Tsouvalas, A.; Metrikine, A.

Important note
To cite this publication, please use the final published version (if applicable).
Please check the document version above.

Contents lists available at ScienceDirect

Engineering Structures

Magnetomechanical response of a steel monopile during impact pile driving

P.C. Meijers [*], A. Tsouvalas, A.V. Metrikine

Delft University of Technology, Faculty of Civil Engineering and Geosciences, Stevinweg 1, 2628 CN Delft, the Netherlands

A B S T R A C T

This paper reports on a measurement campaign in which the magnetomechanical response of a steel monopile is recorded during installation with a hydraulic impact hammer. By comparing impact-induced changes in the magnetic stray field of the structure to the measured strain, this effect is analysed for the first time under dynamic loading conditions on such a large scale. It is shown that the measured stray field displays an excellent correspondence with the strain in terms of frequency content and amplitude ratio for hammer blows that induce compressive strain pulses of different magnitude. Using the data, a non-contact method is developed and validated to infer the hammer-induced strains using the dynamic magnetic stray field. The proposed method can be applied during pile installations when the use of conventional strain measurement devices is challenging, e.g. in the offshore environment.

1. Introduction

In recent years, the number of offshore wind turbines commissioned has increased significantly due to a surge in the demand for energy from renewable sources [1]. Despite the plethora of available foundation types to support the wind turbines, steel monopiles are the preferred choice in the relatively shallow North Sea [2]. Monopiles are thin-walled cylindrical structures with a diameter of several meters and a length of tens of meters, and they comprise about 70% of the newly-installed foundations in European waters in 2019 [3]. To drive these large-scale structures to the desired penetration depth into the seabed, hydraulic impact hammers are most commonly employed, which administer several thousands of hammer blows during a typical monopile installation. Each hammer blow generates a compressive stress pulse that propagates downwards from the pile top; this provides sufficient energy to overcome the soil resistance, allowing the pile to progress further into the seabed.

Currently, it is common practice to monitor the impact-induced strains and accelerations during pile installations. Such measurements, which are taken a few meters below the pile head, allow one, by means of signal matching, to monitor the pile driving process [4] and to determine the bearing capacity [5]. Moreover, the collected data can be used to reliably predict the generated underwater noise [6] and to estimate the consumed fatigue life [7]. Normally, the latter is estimated based on the measured strain signals in conjunction with a stress wave propagation model similar to the driveability model proposed by Smith

[8]. For large-diameter piles, this driveability model needs to be modified to correctly predict the stress wave propagation [9] and the soil resistance [10].

To obtain the aforementioned beneficial information, continuous monitoring during offshore pile installations using contact sensors is routinely employed nowadays [11,12]. However, attaching a sensor to the structure may be onerous and time consuming, especially in the hostile marine environment [13,14]. Moreover, to infer elastic strain and plastic deformation caused by a hammer blow, a sensor is required in the vicinity of the pile head, where the large strains develop. Unfortunately, the hammer-induced forces can damage these sensors, making strain or acceleration measurements directly at the pile head challenging [15]. To circumvent these limitations, a method which allows to monitor the pile response with a non-contact measurement device is highly desirable.

Several classes of non-contact methods to determine the deformation of a structure exist. One commonly applied method uses optical signals, e.g. a laser speckle imaging sensor can be applied to measure the flexural deformation of concrete sleepers used in railways [16]. Another optical technique that has received considerable interest over the past years, is Digital Image Correlation (DIC) [17], with the main benefit being the fact that it provides full field strain data over the considered surface area. However, applying this latter technique to a system subjected to dynamic loads requires the use of expensive high-speed cameras [18], which might be strenuous and too costly to employ offshore. Furthermore, DIC relies on optical markings on the structure's surface,

---

requiring a careful preparation of the area of interest [19,20]. Again, such an endeavour is far from trivial in the marine environment.

To circumvent these shortcomings, a different class of non-contact methods is considered in this paper; one that takes advantage of the ferromagnetic nature of the structure via the magnetomechanical effect. In the presence of the geomagnetic field, a steel structure is weakly magnetised, i.e. it has a magnetisation, which is (not exclusively) sensitive to elastic [21] and plastic deformation [22]. The interactions between mechanical and magnetic quantities are colloquially known as the magnetomechanical effect. As the magnetic stray field generated by the structure's magnetisation permeates the space surrounding it, a magnetic field measurement in its vicinity provides a non-contact method to infer deformations of the ferromagnetic structure.

To date, most experimental research on the magnetomechanical effect has been performed at a laboratory scale. While most of these experiments focus on the response of ferromagnetic specimens under quasi-static external forcing [23–26], some researchers have recently investigated specimens subjected to dynamic loading [27,28]. Nonetheless, limited data is available on the in situ magnetomechanical response of large-scale structures in a weak ambient magnetic field. Moreover, available in situ experiments focus solely on statically loaded structures, e.g. steel pipelines under inspection [29,30]. More recently, the bending strength of corroded reinforced concrete beams was determined with a method that employs the structure's magnetic stray field [31]. However, all the aforementioned in situ experiments pertain quasi-static loading conditions, which are incomparable with the dynamic loadings encountered during monopile installations. Therefore, the aim of this paper is to fill this gap by presenting the in situ measured magnetomechanical response of a monopile during installation, and demonstrate how these measurements could serve as the basis for the development of a non-contact technique to infer the impact-induced deformations.

The paper is structured as follows. First, the set-up of the in situ measurement campaign to collect the magnetomechanical data under dynamic loads is detailed. Second, the correlation function and the data processing algorithm are described, which enable one to conveniently analyse the data from a large number of hammer blows. Third, the processed measurement results are discussed with the emphasis being placed on the correlation between the stray field changes and the strain both in terms of frequency content and amplitude. Based on this discussion, the practical application of the non-contact measurement device to infer the impact-induced strains during a pile installation is treated. Finally, the main conclusions are briefly summarised under the prism of future developments in the field.

2. Experimental set-up

In July 2019, a steel cylindrical pile was installed at the yard of IHC-IQIP in Sliedrecht, the Netherlands. The installed pile comprises of cylindrical steel sections with a height of 3 m each, which are stacked on top of each other by means of circumferential welds. The dimensions and material properties of the installed pile are summarised in Table 1, in which h denotes the wall thickness, R is the outer radius, and L represents the length of the pile. Moreover, E_p is Young's modulus, ρ_p denotes the density and ν_p is Poisson's ratio. During the final stage of the installation, i.e. the last 141 hammer blows, the measurement system

was deployed, which is shown in Fig. 1a. The pile was driven by a S350 hydraulic hammer, which is capable of delivering a blow with an impact energy up to 350 kJ.

A schematic of the measurement system is presented in Fig. 1c and d, which indicates the cylindrical coordinate system used to define the sensor positions and the directions of the measured magnetic field components. The radial, circumferential and axial directions are designated r, θ, and z, respectively. Moreover, the external magnetic field of the Earth $\mathbf{B}^0$ is marked in Fig. 1c and d; it is considered to be time- and space-invariant. At the installation site, the z-component of the geomagnetic field dominates, i.e. the magnetic field points strongly downwards. In the top view of the pile (Fig. 1d), the angle between the geomagnetic field vector and the r-axis is $\beta \approx 33°$.

It is important to note that, prior to installation, the pile was not subjected to any magnetic treatment, i.e. no (de) magnetisation procedure of the structure was performed. Employing such a process is not feasible in an offshore environment (or even in an onshore setting given the large scale), as it requires the generation of carefully controllable magnetic fields by means of magnetising coils.

For the simultaneous measurement of the strain-induced magnetic stray field changes in the vicinity of the structure at different locations, a dedicated measurement system was developed to support several bi-axial magnetometers (type: HMC1022). Each bi-axial magnetic sensor is placed a certain distance d (indicated in Fig. 1) from the surface of the pile. Additionally, two different configurations for positioning of the magnetometers are employed: sleeve-based (S) and ground-based (G). In the former configuration, the sensor is attached to a PVC frame which is directly connected to the sleeve of the hammer (Fig. 1a). Due to the frame, the sleeve-based sensors retain their relative position a (Fig. 1c) with respect to the pile head during the tests. In the second configuration, the sensors are mounted on top of non-magnetic tripods which are placed directly on the ground. As a result, the relative position between the sensor and the pile changes when the pile penetrates further into the soil. In the remainder of this paper, the data obtained with ground-based configuration are not discussed, since this sensor arrangement predominantly provides valuable information for real-time monitoring of the penetration of the pile [32], which is not the focal point of this work.

Next to the magnetic stray field measurement, strains in the structure are recorded by two Pile Driving Analysers (PDAs) which are directly attached to the pile surface using an adhesive. These devices are positioned diametrically, and each one consists of a strain measurement device (type: *TML* FLA-2.350–11) and an accelerometer (type: Endevco 7270A) to measure the strain and acceleration in the axial direction, i.e. along the z-axis. Fig. 1b shows a close-up of one of the PDA sensors (PDA1). As the magnetomechanical effect results from the varying strain, only measured strain data are considered throughout this paper.

Table 2 summarises the sensors deployed during the measurement campaign, including their circumferential position θ, axial position a, and (for the magnetometers) the distance d from the surface of the pile. As mentioned, four bi-axial magnetometers are attached to the sleeve (S1 to S4), and they completely enclose the circumference of the pile as the sensors are placed 90° apart. Fig. 1d shows the circumferential positions of these sensors with respect to the geomagnetic field direction. In Table 2, the index i indicates the number of the hammer blows in which the sensor was active (a total of 141 blows were registered). Both magnetic and mechanical data were sampled with a frequency of 50 kHz to correctly capture the dynamic response of the pile to the hammer blows.

3. Data processing

Given the broad spectrum of the measured quantities, direct comparison of the raw data does not provide a feasible framework to analyse the magnetomechanical response of the system during pile driving. Thus, the full time signals are reduced to a selected number of

Table 1
Dimensions and material properties of the steel monopile installed during the in situ measurement campaign in Sliedrecht, the Netherlands.

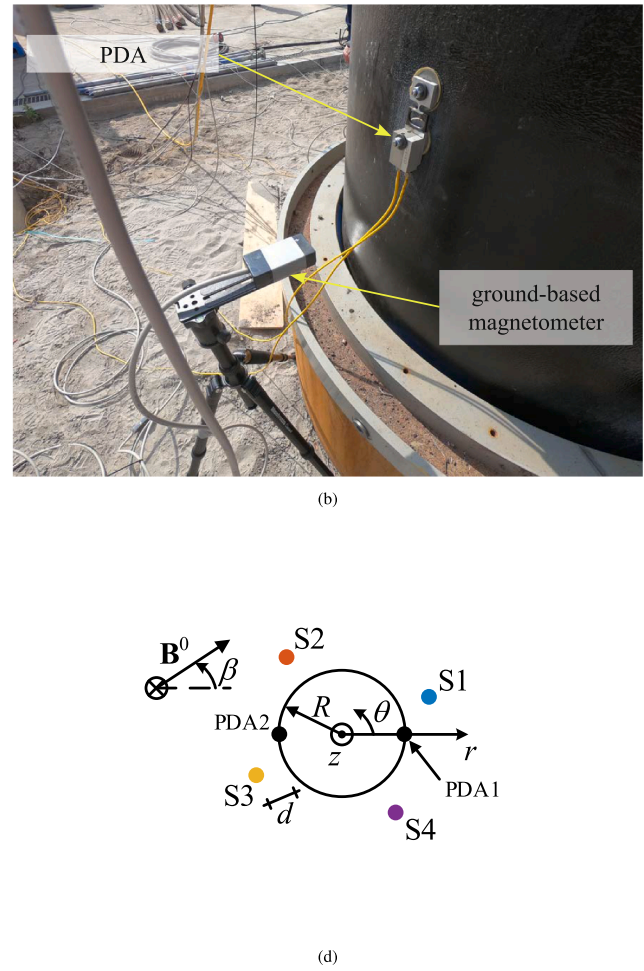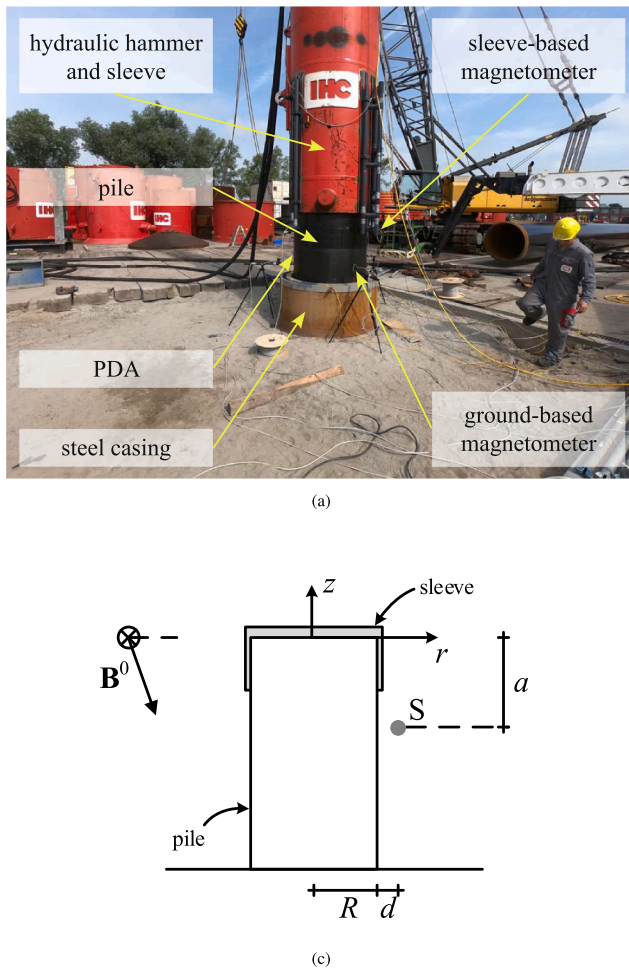| Parameter	Value	Parameter	Value
h	0.050 m	E_p	210 GPa
R	0.6096 m	ρ_p	7850 kg/m³
L	62.0 m	ν_p	0.3

Fig. 1. Overview of the measurement system during installation of the pile. (a) Annotated photograph of the installation set-up. (b) Close-up of a ground-based sensor and PDA1. (c) Schematic side view. (d) Schematic top view.

Table 2
Overview of the measurement system. For each sensor, the measured quantities are listed; the index i specifies the registered number of impacts in which the listed sensor was active; θ and a are the circumferential and axial positions, respectively; for the bi-axial magnetometers, the distance from the surface of the pile is denoted by d.

Sensor	Measurement	i	θ [°]	a [m]	d [m]
S1	B_z, B_r	1–141	20	2.75	0.20
S2	B_z, B_r	1–141	110	2.75	0.20
S3	B_z, B_r	1–141	200	2.75	0.20
S4	B_z, B_r	1–141	290	2.75	0.20
PDA1	ε_z	1–83	0	3.50	–
PDA2	ε_z	1–7	180	3.50	–

parameters for each hammer blow. Moreover, the normalised correlation coefficient is introduced to quantify the correspondence between the stray field and the strain. Subsequently, the principle component analysis of the stray field is detailed.

3.1. Event data

Considering the relatively large number of hammer blows and the resulting amount of data, it is more practical to define characteristics for each of the magnetomechanical quantities that typify the time signals recorded by the sensors during each individual hammer blow, which can

be seen as discrete events in the full data set. For impact i, the hammer registers the impact time τ_i, which is the time instance the ram of the hammer is released, and the supplied hammer energy E_i. Fig. 2 shows typical signals of the magnetic stray field and the axial strain directly after $t = \tau_i$. Using τ_i, a time interval t_i ensuing the impact is defined as follows:

$$t_i = [\tau_i, \ \tau_i + \Delta t], \tag{1}$$

in which Δt is a time interval which is approximately ten times the duration of the initial strain pulse, i.e. $\pm 0.050\,\mathrm{s}$ for the case study here.

Fig. 2a shows the axial component of the full magnetic field vector $\mathbf{B}(t)$. It is noted that, even in the absence of mechanical loading, the magnetic field in the vicinity of the pile is non-zero, since the structure's magnetisation generates a magnetic stray field that permeates the region around it. Assuming that at $t = \tau_i$ the structure is unloaded (the static load caused by the mass of the impact hammer resting on the pile is assumed to be negligible), the remanent stray field value $\overline{\mathbf{B}}_i$ is equal to the magnetic field in the unloaded state:

$$\overline{\mathbf{B}}_i = \mathbf{B}(\tau_i). \tag{2}$$

On the vertical axis of Fig. 2a, this remanent value is marked. As a result of strain-driven reordering of the internal magnetic domains, the remanent stray field value could change in between impacts when sufficient energy is supplied to the system [33,34]. Additionally, external factors, e.g. a steel object temporarily approaching the sensor, can further alter this value.
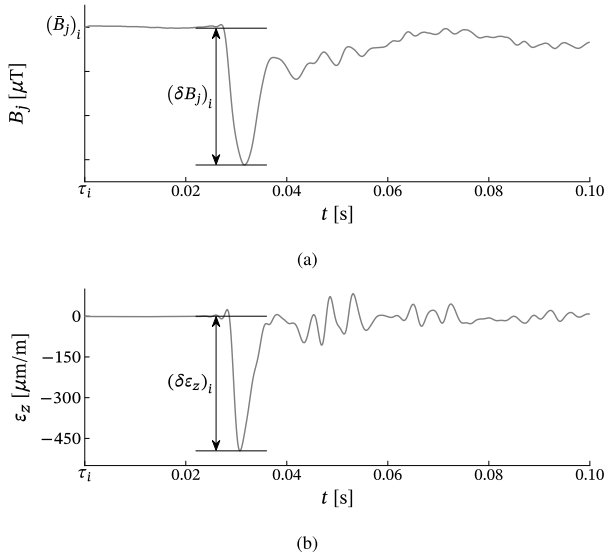
(a)

(b)

Fig. 2. Exemplary time signals of (a) a component of the magnetic stray field and (b) the axial strain ε_z measured during a single hammer blow i with three relevant characteristic parameters indicated: the remanent stray field value $\left(\overline{B}_j\right)_i$, the maximum magnetic variation from the remanent field $(\delta B_j)_i$, and the peak strain $(\delta \varepsilon_z)_i$.

During a hammer blow, the generated strain pulse changes the structure's magnetisation through the magnetomechanical effect. The resulting variations in the magnetic stray field are small compared to the remanent value. Hence, it is useful to separately define the magnetic field variation $\Delta \mathbf{B}_i(t_i)$ as follows:

$$\Delta \mathbf{B}_i(t_i) = \mathbf{B}(t_i) - \overline{\mathbf{B}}_i. \tag{3}$$

This quantity reveals the deviations of the stray field from the unstrained state of the system, and, consequently, it is expected to reflect solely the strain-induced magnetisation changes. Given the clear peak in the magnetic signal in Fig. 2a, it is natural to define the maximum deviation from the remanent value as a new quantity: the maximum deviation from the remanent field $\delta \mathbf{B}_i$. Note that, for example, a compressive strain—i.e. negative strain—does not necessarily lead to a negative magnetic field change. Thus, to correctly capture the extreme value of the magnetic field variation, one needs to consider the largest deviation from the remanent field (either positive or negative):

$$\left(\delta B_j\right)_i = \max\left(\left\|\left(\Delta B_j\right)_i(t_i)\right\|\right)\mathrm{signum}\left(\left(\Delta B_j\right)_i(t_i)\right) \tag{4}$$

in which j specifies the vector component. The former expression ensures that the largest deviation from the remanent field is selected while retaining its sign. As an example, Fig. 2a indicates $(\delta B_j)_i$ for a hammer blow.

Similar quantities can be defined to characterise the strain signal $\varepsilon_z(t_i)$. Assuming no permanent structural deformation at the location of the strain sensor, the structure is unstrained before each impact, eliminating the need to specify the remnant strain value for each hammer blow. By applying an expression similar to Eq. (4) to $(\varepsilon_z)_i$, the peak of the strain signal $(\delta \varepsilon_z)_i$ is obtained as shown in Fig. 2b.

To summarise, for each impact i, four distinct impact characteristics are considered:

(i) impact energy E_i;
(ii) peak strain value $(\delta \varepsilon_z)_i$;
(iii) remanent magnetic field $\overline{\mathbf{B}}_i$;
(iv) maximum deviation from the remanent field $(\delta B_j)_i$.

Note that the latter two quantities are determined for each component of the stray field. For brevity, the subscripts i are dropped in the sequel, keeping in mind that the impact characteristics above are examined at discrete time moments.

3.2. Normalised correlation coefficient

To examine whether the magnetic stray field can be used to infer the hammer-induced strain in a non-contact manner, the correspondence between the strain and magnetic stray field components is quantified by means of the normalised correlation coefficient. For two real valued functions $u(t)$ and $v(t)$, the normalised correlation function is defined as [35]:

$$\rho_{uv}\left(t\right) = \frac{1}{\sqrt{E_u E_v}} \int_{-\infty}^{\infty} u(\tau - t)v(t)\,\mathrm{d}\tau, \tag{5}$$

in which

$$E_u = \int_{-\infty}^{\infty} u(\tau)^2\,\mathrm{d}\tau, \qquad E_v = \int_{-\infty}^{\infty} v(\tau)^2\,\mathrm{d}\tau, \tag{6}$$

are the expected values for the two functions. When the function $u(t)$ and $v(t)$ are only defined on a finite time interval, as is the case for the magnetic and strain signals, the integration limits are equal to the bounds of the relevant interval. The normalised correlation function is a function of a time shift, and it takes a maximum value when the time-shifted version of $u(t)$ matches $v(t)$. Consequently, a useful parameter to quantify the correlation is the normalised correlation coefficient:

$$c_{uv} = \max(\|\rho_{uv}(t)\|). \tag{7}$$

When $c_{uv} = 1$, the signals are perfectly correlated; when the time series are completely dissimilar, $c_{uv} = 0$. In case $u(t)$ and $v(t)$ are perfectly correlated, $u(t) = \alpha v(t)$, i.e. $v(t)$ is a scaled version of $u(t)$, and α is a scalar proportionality constant. The latter incorporates the sign difference between the amplitudes of the signals, hence the absolute value of $\rho_{uv}(t)$ suffices in Eq. (7). Note that, in case $c_{uv} = 1$, the two signals have an identical frequency content as well, since they only differ in amplitude.

3.3. Principle component analysis

Each bi-axial magnetometer registers the radial and axial component of the stray field (Table 2), i.e. B_r and B_z, respectively. Given these two components, the magnetic variation $\Delta \mathbf{B}(t)$ can be decomposed into its principle components as follows:

$$\Delta \mathbf{B}(t) = \Delta B_r(t)\mathbf{r} + \Delta B_z(t)\mathbf{z} = \Delta B_1(t)\mathbf{e}_1 + \Delta B_2(t)\mathbf{e}_2, \tag{8}$$

in which $\mathbf{r}, \mathbf{z}, \mathbf{e}_1$ and $\mathbf{e}_2$ represent the unit vectors along the radial, the axial, the major principle and the minor principle axis, respectively. Along each of these directions, $\Delta B_r(t), \Delta B_z(t), \Delta B_1(t)$ and $\Delta B_2(t)$ denote the respective variations of the stray field. To illustrate this decomposition, Fig. 3 shows $\Delta \mathbf{B}(t)$ measured by S4 during impact 7. It is easily verified that the maximum variability is directed along the major principle axis $\mathbf{e}_1$, which is the essence of the principle component analysis (PCA) [36]. Thus, by re-expressing the dynamic stray field along the principle axes, only the first principle component has to be considered to analyse the dynamic magnetomechanical response of the structure. Next to the dimensional reduction of the data, the PCA removes the ambiguity regarding the direction of the transient stray field. The latter is unknown a priori; nevertheless, it is expected to spatially vary together with the remanent magnetisation of the structure. As the PCA is completely data-driven [36], it provides an objective way to extract a single magnetic variable that captures the desired dynamic response regardless of the dominant measured component. Naturally, similar to the recorded field components, a maximum deviation δB_1 can be extracted from $\Delta B_1(t)$.
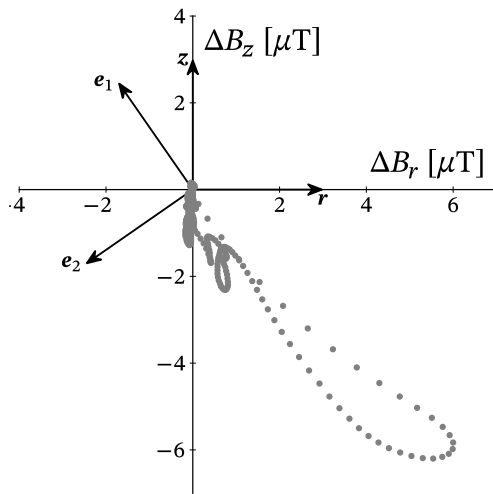
Fig. 3. Magnetic variation $\Delta\mathbf{B}$ measured by S4 during impact 7, in which $\mathbf{r}$ and $\mathbf{z}$ denote the unit vectors of the respective measured radial and axial components of $\Delta\mathbf{B}$. Unit vectors $\mathbf{e}_1$ and $\mathbf{e}_2$ are directed along the major and minor principle axis, respectively.

4. Results and discussion

Several aspects of the measured mechanical and magnetomechanical response of the pile are discussed below. First, the strain signals obtained with the conventional contact sensors are analysed since these serve as a reference for comparison with the strain-induced stray field. Second, the correlation between the magnetic field variations and the strains is discussed. Third, the magnetomechanical response itself is analysed by means of the characteristics defined in Section 3.1. Finally, a non-contact method is proposed to infer the strain from the measured stray field during pile driving.

4.1. Hammer-induced strains

As indicated in Table 2, two conventional strain measurement devices (PDAs) were diametrically attached to the surface of the pile. Unfortunately, after only seven hammer blows, PDA2 detached from the pile, leaving only PDA1 functioning. The premature failure of PDA2 accentuates the potential benefit of non-contact sensors over classical contact-based devices to monitor the strain levels in the pile. Due to the malfunctioning of PDA2, the discussion in this paper is predominantly based on the data obtained from PDA1.

Fig. 4 presents the time–frequency analysis of typical signals measured during impact 7. Directly following the initial compressive strain pulse, the axial strain signals of PDA1 (Fig. 4a) and PDA2 (Fig. 4d) display high-frequency oscillations that dominate the measurements. The pronounced peaks in the amplitude spectra confirm their presence; around 800 Hz for PDA1 (Fig. 4b), and approximately 550 Hz and 1400 Hz for PDA2 (Fig. 4e). These rapid fluctuations persist much longer ($\Delta t \approx 200$ ms) than the expected duration of an impact-induced strain pulse ($\Delta t \approx 10$ ms). Moreover, these peaks are absent in the time-–frequency analysis of the axial component of the magnetic stray field (Figs. 4g and 4h). Consequently, it is reasonable to assume that the oscillations have a different cause than the actual structural vibrations; most probably, they stem from the vibrations of the wire connected to the device. To eliminate these undesired artefacts from the signals, which do not represent physical strains in the structure, a low-pass filter with a cut-off frequency of 450 Hz is applied to the recordings. Figs. 4c and 4f compare the original and filtered strain signals for PDA1 and PDA2, respectively, revealing that, after an initial compressive strain pulse, only relatively small strains are present in the structure. Since these high-frequency oscillations were originally absent in the stray

field, the magnetic signal is largely unaffected by the applied filter (Fig. 4i).

From the filtered strain signals, the peak strains $\delta\varepsilon_z$ are extracted for PDA1 using the procedure described in Section 3.1. Fig. 5a presents the results for impacts 1 to 83 together with the impact energy registered by the hammer. Apart from their sign, the quantities appear to follow a similar trend. According to the elastic theory of impacting bars [37], the peak strain is expected to be proportional to the square root of the impact energy E. The use of this one-dimensional theory is justified here by the fact that a hammer blow excites frequencies well below the ring frequency f_r of the structure, i.e.:

$$f_r = \frac{1}{2\pi R}\sqrt{\frac{E_p}{\rho_p\left(1-\nu_p^2\right)}} = 1416\,\text{Hz}. \tag{9}$$

The amplitude spectra presented in Fig. 4 indicate that the hammer mainly excites frequencies below 450 Hz. Hence, a one-dimensional theory suffices to describe the axial wave propagation in a monopile in this case [15].

To determine the relation between the peak strain $\delta\varepsilon_z$ and the square root of the impact energy $\sqrt{E}$ from the experimental data, Fig. 5b shows a plot of these two quantities. A linear fit to the data confirms that the assumed proportionality applies, namely:

$$\delta\varepsilon_z \approx -1.33\sqrt{E}, \tag{10}$$

verifying that the elastic one-dimensional theory is adequate in this case. Note that, in the above expression, the proportionality constant has units $\mu\text{ms/m}^2\text{kg}^{0.5}$, since $\delta\varepsilon_z$ is expressed in $\mu\text{m/m}$ and E in kgm^2/s^2. With Eq. (10), the hammer energy can be used to estimate $\delta\varepsilon_z$ in absence of an actual strain measurement, which is the case from impact 84 onwards.

To assess whether the shape of the hammer-induced strain pulse is axially symmetric, the correlation coefficients for the strain signals collected by PDA1 and PDA2 during impact 7 are determined (Table 3). The strain signals correlate extremely well ($c > 0.93$ in all recordings), which suggests that the induced strains at the considered diametric positions are nearly identical in terms of the exited frequency range. This, in turn, indicates that the hammer force is introduced evenly along the circumference of the pile top. Consequently, it seems reasonable to assume that each hammer blow generates an axi-symmetric compressive strain field.

4.2. Correlation between strain and magnetic stray field measurements

For impact 7, Table 3 presents the normalised correlation coefficients for the axial strains and the magnetic measurements along the major principle component ΔB_1. Note that the correlation table is symmetric; only the upper half is presented. From the data, the following is concluded:

  (i) the two strain signals are similar ($c = 0.96$), as previously confirmed in Section 4.1;
 (ii) magnetometer pairs that are placed diametrically (e.g. S1 and S3) exhibit a higher mutual correlation than compared to the sensors located 90° from it, e.g. compare S1 and S3 ($c = 0.94$), S1 and S2 ($c = 0.87$), S2 and S4 ($c = 0.99$), and S3 and S4 ($c = 0.84$);
(iii) the magnetic field signals of S2 and S4 strongly correlate with the strain ($c > 0.78$);
 (iv) for S1 and S3, the correlation between the stray field and the strain is less pronounced ($c > 0.56$).

Given the direction of the geomagnetic field, which is $\beta \approx 33°$ (Fig. 1d), the radial component of S1 and S3, at $\theta = 20°$ and $\theta = 200°$, is almost aligned with the external field, while the radial component of S2 and S4, at $\theta = 110°$ and $\theta = 290°$, is perpendicular to it. Acknowledging this fact, the above observations show that the orientation of the
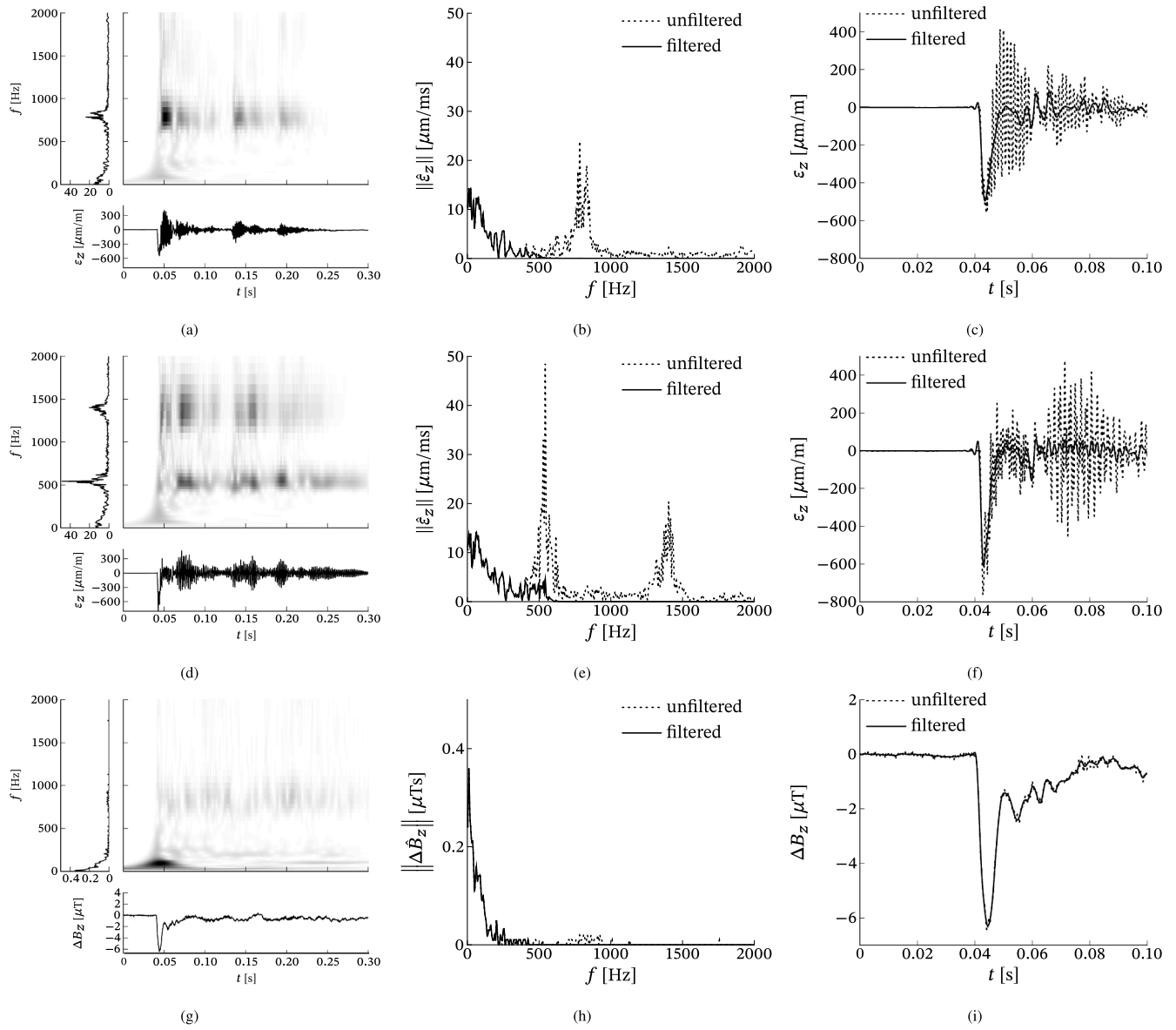
Fig. 4. Time–frequency analysis of the signals measured during a single hammer blow (impact 7). The filtered signals are obtained with a low-pass filter with a cut-off frequency of 450 Hz. (a) Time–frequency plot of PDA1. (b) Amplitude spectrum of PDA1. (c) Time series of PDA1. (d) Time–frequency plot of PDA2. (e) Amplitude spectrum of PDA2. (f) Time series of PDA2. (g) Time–frequency plot of the axial component of S4. (h) Amplitude spectrum of the axial component of S4. (i) Time series of the axial component of S4.
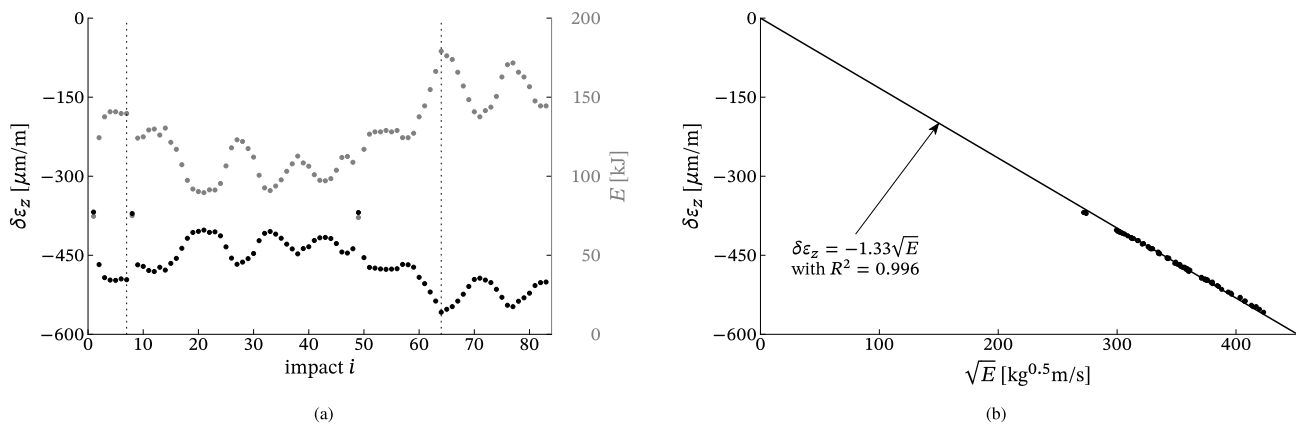

Fig. 5. Analysis of the measured peak strain and the impact energy registered by the hammer. (a) Peak strain (black) and impact energy (grey) for each hammer blow. (b) Peak strain against the square root of the impact energy including a linear fit to the data.

Table 3

Normalised correlation coefficients for the strains and the major principle component of the magnetic signals for impact 7. The table is symmetric, however, only the upper half is shown for clarity.

	PDA1	PDA2	S1	S2	S3	S4
PDA1	1	0.96	0.64	0.86	0.65	0.89
PDA2		1	0.56	0.78	0.57	0.81
S1			1	0.87	0.94	0.85
S2				1	0.86	0.99
S3					1	0.84
S4						1

magnetometer with respect to the external field partly determines the similarity with the impact-induced strains. Since the latter are axially symmetric, the observed magnetomechanical response is caused by the spatial variation of the structure's magnetisation, which is not axially symmetric due to the presence of the external field.

The data presented in Table 3 only pertain to a single hammer blow. To obtain a more general picture, Fig. 6 shows the normalised correlation coefficients between the axial strain measured by PDA1 and the major principle component of the magnetic stray field for the first 83 impacts. Again, for the signals measured by S2 and S4 (with a radial component perpendicular to the external field), the correlation is high ($c > 0.8$); while for S1 and S3 (with a radial component aligned to the external field), the correlation is less pronounced, albeit still reasonable ($c > 0.6$). This confirms the aforementioned dependency of the measured magnetomechanical response on the circumferential position relative to the geomagnetic field direction.

4.3. Analysis of the impact characteristics

Up to now, the discussion focused on the comparison between the stray field and the strains in terms of the normalised correlation coefficient. However, this does not provide any information regarding the actual amplitude of the changes or the remanent stray field values. In this section, the physical characteristics of these measurements are further analysed.

In Fig. 7a, the remanent magnetic field $\overline{B}_r$ displays little variation over the course of the reported impacts. However, $\overline{B}_z$ (Fig. 7b) does exhibit a slight decrease at all four positions, which, at first instance, is not to be expected since the sleeve-based sensors retain their relative position with respect to the pile. A careful examination of the set-up (Fig. 1) shows that this is caused by the penetration of the pile, which moves the sensors closer to the edge of the protective steel casing (Fig. 1a); the latter has a significant magnetic stray field of its own. This additional stray field simply adds to the external field, and makes the latter spatially varying.

To assess the amplitude of the dynamic stray field, Fig. 7c presents the maximum variation of the major principle component δB_1. For each
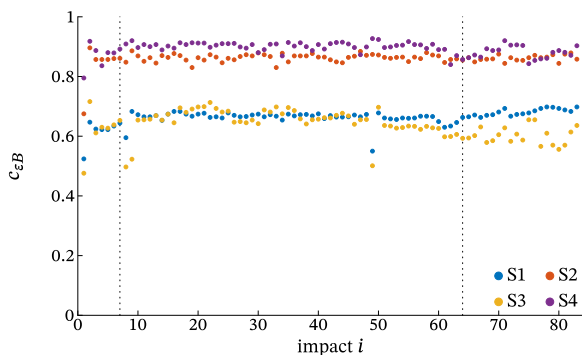

Fig. 6. Normalised correlation coefficients between the axial strain and the major principle component of stray field.

magnetometer, the strain-induced amplitude is different, which is to be expected given the spatially-varying magnetisation of the structure. Nevertheless, δB_1 displays a trend that resembles that of the peak strain (Fig. 7d). To examine this correspondence in more detail, Fig. 8 plots the two quantities versus each other for the two sensors with the highest correlation with the strain, i.e. S2 and S4. The arrangement of the points suggests that the peak strain and the maximum deviation are directly related as follows:

$$\delta B_1 \approx \alpha \delta \varepsilon_z, \tag{11}$$

in which α is a calibration coefficient. The latter is determined by means of linear regression, yielding $\alpha = 12.3 \cdot 10^{-3}$ T and $\alpha = 15.2 \cdot 10^{-3}$ T for S2 and S4, respectively. In addition to the excellent correlation of the full time series of these two quantities as discussed earlier, the above linear relation implies that the dynamic stray field corresponds one-to-one with the hammer-induced strains in the current set-up. Consequently, this expression serves as a basis for a method to infer the strains during a pile installation using non-contact stray field measurements.

4.4. Inference of hammer-induced strains using non-contact stray field measurements

By inverting the expression derived in Eq. (11), the peak axial strain can be inferred from the maximum deviation of the major principle component of the stray field. For the two magnetometers with the best correlation to the strain (S2 and S4), the estimated peaks strains $\widetilde{\delta \varepsilon}_z$ are presented in Fig. 9a in conjunction with the measured peak strains $\delta \varepsilon_z$. For impacts 1–83, the latter are directly obtained from PDA1, while, from impact 84 onwards, the peak strains are computed from the registered impact energy by applying Eq. (10). For impacts 1–95, the inferred strain values correspond reasonably well with the peak strain obtained using the conventional methods, since the error in that impact range is generally less than 10% (the grey band in Fig. 9b). The error becomes large (≫10%) for impact 96 and higher, which results from the change in the remanent stray field due to the sensors approaching to the protective steel casing (Fig. 1a). To illustrate the evolution of the remanent field, Fig. 9c shows the deviation of the four remanent values from the average remanent value for impacts 1–83 (indicated by $\langle \overline{B}_j \rangle$). Initially, the remanent values meander around the average; however, from impact 84 onwards, the values diverge significantly, which co-incides with the deterioration of the quality of the estimated peak strains. Clearly, the α-coefficient is sensitive to permanent changes of the remanent stray field.

Permanent stray field changes reflect irreversible changes of the magnetisation of the structure, for which three situations are relevant here:

(i) when the magnetisation is not yet at a magnetic equilibrium, e.g. at the start of the pile installation, elastic deformation pushes the magnetisation towards this equilibrium. Ordinarily, this state is reached when the load is repeated a few times. As a typical monopile requires several thousands of hammer blows to reach the desired penetration depth, the pile attains the magnetic equilibrium early in the installation process;

(ii) when a ferromagnetic object approaches the magnetometer, e.g. the steel casing in the current set-up. Normally, such an auxiliary structure is not present during a monopile installation;

(iii) when a region of plastic deformation develops in the vicinity of the magnetometer.

Thus, for optimal results, a calibration procedure for α should be performed as soon as the remanent stray field stabilises. Naturally, this coefficient should also be recalibrated in case the sensor is repositioned relative to the pile.

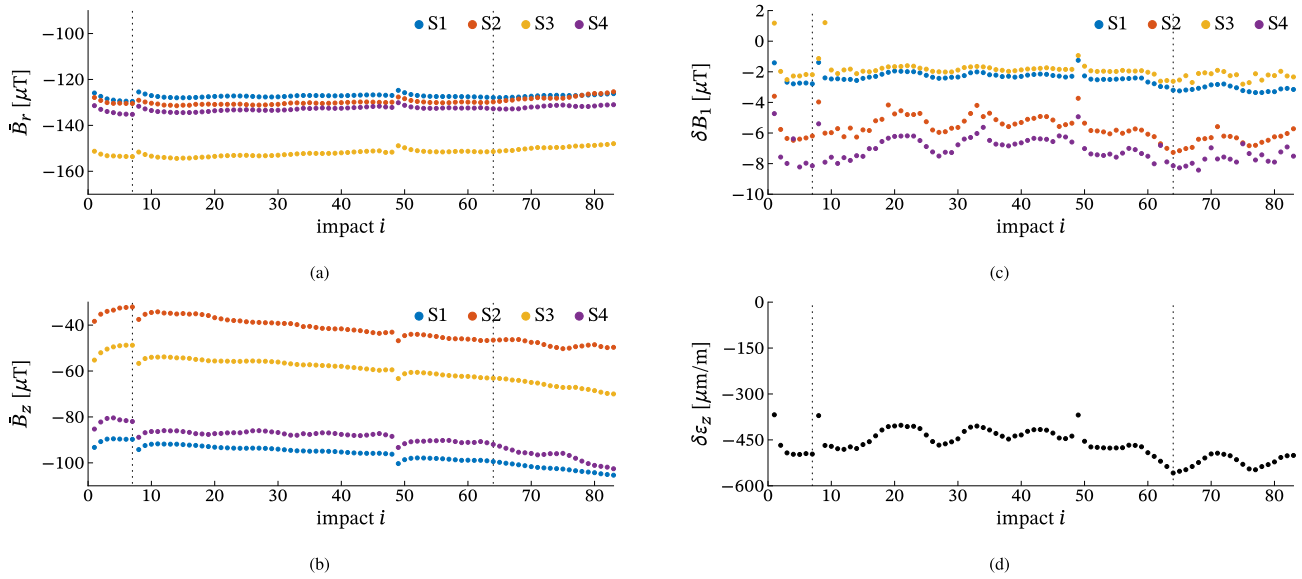Assuming that the properties of the hammer-sleeve assembly are

Fig. 7. Characteristics extracted for impacts 1–83 recorded by the sleeve-based sensors. (a) Radial component of the remanent stray field. (b) Axial component of the remanent stray field. (c) Maximum deviation of the major principle component of the dynamic stray field. (d) Peak strains.
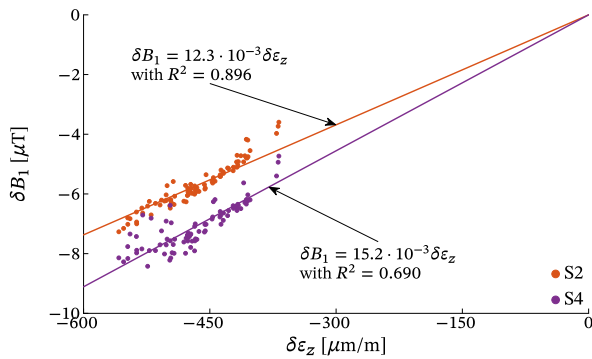

Fig. 8. The maximum variation of the major principle component versus the peak strain for S2 and S4 in conjunction with a linear fit to the data.

constant and that one-dimensional stress wave theory applies, the constant in Eq. (10), which relates the peak strain to the square root of the hammer energy, is uniquely defined by the geometry of the pile and the properties of the hammer-sleeve assembly. Thus, if those parameters are known, the proportionality constant in Eq. (10) can be estimated either by using a temporarily-installed conventional PDA device or by means of numerical simulations. Subsequently, (re) calibration of Eq. (11) entails gradually increasing the hammer energy to its maximum capacity and extracting the peak value of the deviation from the remanent field δB_1 from the full magnetic signals. Then, α can be determined by means of linear regression. Whether this process leads to a robust calibration procedure needs to be investigated in the future.

Since the time series of the strain and the dynamic stray field correlate well ($c > 0.8$), the calibration coefficient α determined for the peak values is equally valid to express the full strain history in terms of the major component of the stray field, as follows:

$$\varepsilon_z(t) = \frac{1}{\alpha}\Delta B_1(t). \tag{12}$$

Fig. 10 shows the resulting time signals for impact 64. Generally, the shape of the inferred strain signals correspond well with the measured signal, as expected from the high correlation coefficient. However, two important points need to be mentioned:

(i) The compressive strain pulse is prolonged in time by an amount of 2 ms. This behaviour stems from the fact that the magnetic stray field is essentially determined by the strain-sensitive magnetisation of the entire structure. Fortunately, due to the decay of the magnetic field with distance, the stray field at the magnetic field sensor is only influenced by structure's magnetisation in its vicinity. Naturally, the strain gauge is only sensitive to the local deformation at the sensor. This difference in sensitivity causes the observed behaviour. For example, although the stress wave has passed the strain gauge, it still influences the stray field at the magnetometer, creating the apparent elongation of the actual pulse. To increase the accuracy of the inferred strain signals, one should compensate for this elongation; this item is not yet studied in this work.

(ii) Directly following the initial compressive strain pulse, the measured strain at $t \approx 0.02$ s fluctuates around zero, while the inferred strain fluctuates around a non-zero value. This discrepancy is not attributed to the stress wave examined, but it is most probably caused by low-frequency vibrations ($f \approx 15$ Hz) of the hammer-sleeve assembly to which the sensor is attached.

Despite these differences, the overall satisfactory correspondence between the inferred and measured strains demonstrates that data from a magnetometer that retains its position relative to the structure can be used to infer the impact-induced strains in the structure using a non-contact sensor.

Naturally, the proposed non-contact method to infer hammer-induced strains is in a preliminary stage, and it needs development before it can be applied to offshore installation of piles. However, the technique proposed here makes no assumption as to the pile dimensions, soil conditions, L/D and D/t ratios, etc., since it is based on the local magnetisation changes of the pile material observed during impact piling. Hence, it is expected to be valid for a wider class of structural systems and loading conditions. Note that the method described in the above provides only a non-contact alternative for the strain measurement of a PDA sensor. The acceleration measurement, which is essential to successfully infer the pile capacity via signal matching, must also be revised. Such an endeavour, however, lies beyond the scope of the current work.

Using magnetometers to infer the hammer-induced strain has certain benefits over the application of conventional sensors, of which the most
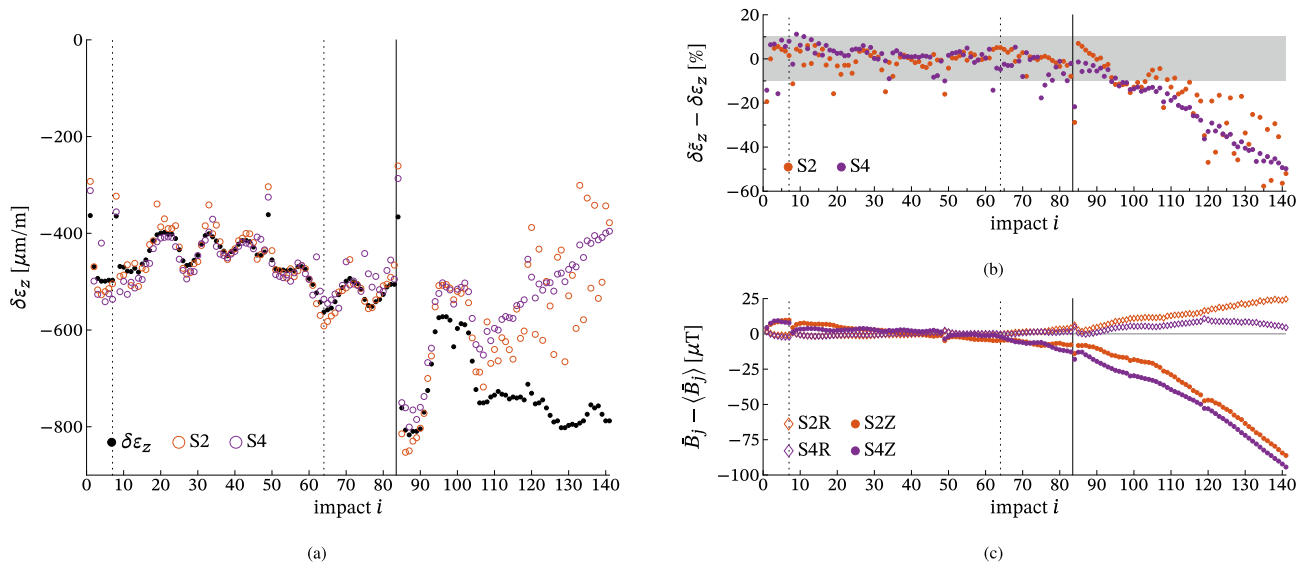
(a)

(b)

(c)

Fig. 9. Peak strain estimation using the measure stray field variations of S2 and S4. For impacts 1–83, the peak strain is directly measured, while, from impact 84 onwards, it is computed from the registered impact energy. (a) Peak strain inferred from the magnetic stray field data using the calibrated relation. (b) Error of the estimated peak strain. The grey band indicates the region with ±10% error. (c) Deviation of the remanent stray field from the average remanent stray field during impacts 1–83.
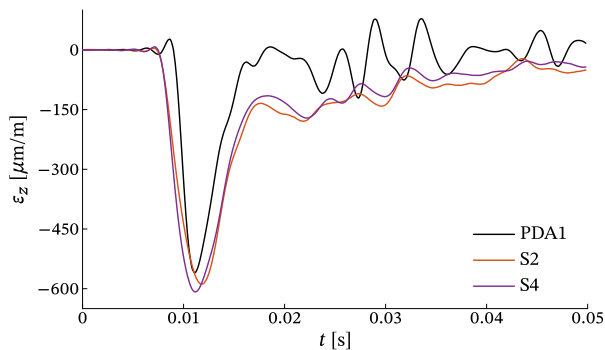

Fig. 10. Measured axial strain for impact 64 compared with the strain inferred from the stray field measurements of S2 and S4.

important was demonstrated by the premature failure of PDA2 during the reported measurement campaign as a result of the high accelerations experienced by that device. Naturally, a non-contact sensor is not exposed to such high contact forces, providing a more robust alternative. Moreover, the deployment of a magnetometer could be rapid and straightforward, perhaps by incorporating the device into the sleeve of the impact hammer, saving valuable time in the tight installation window. Contrary to optical techniques for non-contact strain measurement, the magnetomechanical approach performs equally well underwater, since the stray field is not disturbed by the presence of water, while optical signals will be distorted or blocked by the fluid. Consequently, the proposed magnetic method can be applied during a complete offshore installation, even for subsea structures.

5. Conclusions

A full-scale in situ measurement campaign has been conducted during an onshore monopile installation, resulting in a unique data set that contains the magnetomechanical response of a large-scale structure to high impact loads. Stray field data have been collected with a set of four magnetometers, which are attached to the hammer's sleeve, to ensure that the sensors retain their relative position with respect to the pile throughout the installation. The major principle component of the

measured dynamic stray field shows a strong correlation with the simultaneously measured axial strain ($c > 0.8$). Moreover, for the current set-up, it was shown that the peak strain and the maximum deviation from the remanent stray field are linearly related. Using these two observations, a non-contact method is proposed to infer the hammer-induced strain from the measured stray field data. After calibration, the method yields inferred strain signals that have a satisfactory correspondence with the measured axial strain, provided that the remanent stray field remains constant. It is anticipated that this research can contribute to improving the possibilities for monitoring the strains during the installation of large-scale steel structures.

Declaration of Competing Interest

The authors declare that they have no known competing financial interests or personal relationships that could have appeared to influence the work reported in this paper.

Acknowledgements

References

[1] Jensen KS, Petersen SJ, Pedersen RR. European offshore wind engineering – past, present and future. Proc Inst Civil Eng - Civil Eng 2018;171(4): 159–165. doi: 10.1680/jcien.17.00040.

[2] Doherty P, Gavin K. Laterally loaded monopile design for offshore wind farms. Proc Inst Civil Eng - Energy 2012;165(1): 7–17. doi:10.1680/ener.11.00003.

[3] WindEurope, Offshore Wind in Europe. Key trends and statistics 2019, Tech. rep., WindEurope; 2020.

[4] Rausche F, Nagy M, Webster S, Liang L. CAPWAP and Refined Wave Equation Analyses for Driveability Predictions and Capacity Assessment of Offshore Pile Installations. In: ASME 2009 28th international conference on ocean, offshore and arctic engineering, American Society of Mechanical Engineers, 2009, pp. 375–383.

[5] Webster S, Givet R, Griffith A. Offshore pile acceptance using dynamic pile monitoring. In: Santos JA, editor. The Application of Stress-Wave Theory to Piles: Science, Technology and Practice: Proceedings of the 8th International Conference on the Application of Stress-Wave Theory to Piles: Lisbon, Portugal, 8-10 September 2008. IOS Press; 2008. p. 655–61.

[6] Tsouvalas A. Underwater Noise Emission Due to Offshore Pile Installation: A Review. Energies 2020;13(12):3037. https://doi.org/10.3390/en13123037.

[7] Chung J, Wallerand R, Hélias-Brault M. Pile fatigue assessment during driving. Proc Eng 2013;66:451–63. https://doi.org/10.1016/j.proeng.2013.12.098.

[8] Smith EAL. Pile-driving analysis by the wave equation. Am Soc Civil Eng Trans 1962;127:1145–93.

[9] Meijers PC, Tsouvalas A, Metrikine AV. The effect of stress wave dispersion on the drivability analysis of large-diameter monopiles. Proc Eng 2017;199:2390–5. https://doi.org/10.1016/j.proeng.2017.09.272.

[10] Versteijlen WG, Metrikine AV, van Dalen KN. A method for identification of an effective Winkler foundation for large-diameter offshore wind turbine support structures based on in-situ measured small-strain soil response and 3D modelling. Eng Struct 2016;124:221–36. https://doi.org/10.1016/j.engstruct.2016.06.007.

[11] Wisotzki E, van Foeken R, van Esch P, Novakovic D. Strain and Acceleration Measurements at Instrumentation Distances to the Pile Head of 0.5 and 1.0 Times the Diameter—Offshore Pile-Monitoring Experience. In: Bullock P, Verbeek G, Paikowsky S, Tara D, editors. 10th International Conference on Stress Wave Theory and Testing Methods for Deep Foundations. West Conshohocken, PA: ASTM International; 2019. p. 506–19. https://doi.org/10.1520/STP161120170238.

[12] Buckley RM, Jardine RJ, Kontoe S, Barbosa P, Schroeder FC. Full-scale observations of dynamic and static axial responses of offshore piles driven in chalk and tills. Géotechnique 2020;70(8):657–81. https://doi.org/10.1680/jgeot.19.TI.001.

[13] Anderson MR. Nondestructive testing of offshore structures. NDT Int 1987;20(1):17–21. https://doi.org/10.1016/0308-9126(87)90368-3.

[14] Wang P, Tian X, Peng T, Luo Y. A review of the state-of-the-art developments in the field monitoring of offshore structures. Ocean Eng 2018;147:148–64. https://doi.org/10.1016/j.oceaneng.2017.10.014.

[15] Meijers PC, Tsouvalas A, Metrikine AV. A non-collocated method to quantify plastic deformation caused by impact pile driving. Int J Mech Sci 2018;148:1–8. https://doi.org/10.1016/j.ijmecsci.2018.08.013.

[16] Pang Y, Lingamanaik SN, Chen BK, Yu SF. Measurement of deformation of the concrete sleepers under different support conditions using non-contact laser speckle imaging sensor. Eng Struct 2020;205:110054. https://doi.org/10.1016/j.engstruct.2019.110054.

[17] Franco JM, Caicedo JM, Marulanda J, Sutton M, Thomson P. RGB-D-DIC technique for low-cost 3D displacement fields measurements. Eng Struct 2019;197:109457. https://doi.org/10.1016/j.engstruct.2019.109457.

[18] Gilat A, Seidt J, Matrka T, Gardner K. A New Device for Tensile and Compressive Testing at Intermediate Strain Rates. Exp Mech 2019;59(5):725–31. https://doi.org/10.1007/s11340-019-00488-1.

[19] Yang L, Ding C, Yang R, Lei Z, Wang J. Full field strain analysis of blasting under high stress condition based on digital image correlation method. Shock Vib 2018;2018:1–7. https://doi.org/10.1155/2018/4894078.

[20] Sieffert Y, Vieux-Champagne F, Grange S, Garnier P, Duccini J, Daudeville L. Full-field measurement with a digital image correlation analysis of a shake table test on a timber-framed structure filled with stones and earth. Eng Struct 2016;123:451–72. https://doi.org/10.1016/j.engstruct.2016.06.009.

[21] Atherton DL, Jiles DC. Effects of stress on the magnetization of steel. IEEE Trans Magn 1983;19(5):2021–3. https://doi.org/10.1109/TMAG.1983.1062784.

[22] Bozorth RM, Williams HJ. Effect of small stresses on magnetic properties. Rev Mod Phys 1945;17(1):72–80. https://doi.org/10.1103/RevModPhys.17.72.

[23] Li Z, Dixon S, Cawley P, Jarvis R, Nagy PB, Cabeza S. Experimental studies of the magneto-mechanical memory (MMM) technique using permanently installed magnetic sensor arrays. NDT & E Int 2017;92(Supplement C):136–48. https://doi.org/10.1016/j.ndteint.2017.07.019.

[24] Viana A, Rouve L-L, Cauffet G, Coulomb J-L. Analytical model for external induction variations of a ferromagnetic cylinder undergoing high mechanical stresses in a low magnetic field of any orientation. IEEE Trans Magn 2011;47(5):1366–9. https://doi.org/10.1109/TMAG.2010.2078801.

[25] Yao K, Wang ZD, Deng B, Shen K. Experimental research on metal magnetic memory method. Exp Mech 2012;52(3):305–14. https://doi.org/10.1007/s11340-011-9490-3.

[26] Birss RR, Faunce CA, Isaac ED. Magnetomechanical effects in iron and iron-carbon alloys. J Phys D: Appl Phys 1971;4(7):1040. https://doi.org/10.1088/0022-3727/4/7/322.

[27] Peussa T, Belahcen A. Coupled wave-equation and eddy-current model for modelling and measuring propagating stress-waves. Arch Electr Eng 2015;64(2):215–26. https://doi.org/10.1515/aee-2015-0018.

[28] Leung MSH, Corcoran J, Nagy PB. The influence of the dynamic magnetoelastic effect on potential drop measurements. NDT & E Int 2019;102:153–60. https://doi.org/10.1016/j.ndteint.2018.11.014.

[29] Atherton D, Coathup L, Jiles D, Longo L, Welbourn C, Teitsma A. Stress induced magnetization changes of steel pipes–Laboratory tests. IEEE Trans Magn 1983;19(4):1564–8. https://doi.org/10.1109/TMAG.1983.1062576.

[30] Atherton D, Welbourn C, Jiles D, Reynolds L, Scott-Thomas J. Stress-induced magnetization changes of steel pipes–Laboratory tests, Part II. IEEE Trans Magn 1984;20(6):2129–36. https://doi.org/10.1109/TMAG.1984.1063572.

[31] Qiu J, Zhou J, Zhao S, Zhang H, Liao L. Statistical quantitative evaluation of bending strength of corroded RC beams via SMFL technique. Eng Struct 2020;209:110168. https://doi.org/10.1016/j.engstruct.2020.110168.

[32] Meijers PC, Tsouvalas A, Metrikine AV. Monitoring Monopile Penetration through Magnetic Stray Field Measurements. In: Papadrakakis M, Fragiadakis M, Papadimitriou C, editors. Proceedings of the XI International Conference on Structural Dynamics, Vol. 1. Athens, Greece: EASD Procedia; 2020. p. 1272–80. https://doi.org/10.47964/1120.9102.19534.

[33] Maylin MG, Squire PT. Departures from the law of approach to the principal anhysteretic in a ferromagnet. J Appl Phys 1993;73(6):2948–55. https://doi.org/10.1063/1.353026.

[34] Makar JM, Atherton DL. Effects of isofield uniaxial cyclic stress on the magnetization of 2% Mn pipeline steel - behavior on minor hysteresis loops and small major hysteresis loops. IEEE Trans Magn 1995;31(3):2220–7. https://doi.org/10.1109/20.376241.

[35] Shin K, Hammond J. Fundamentals of Signal Processing for Sound and Vibration Engineers. Hoboken, NJ: Wiley, Chichester, England; 2008. p. 227–9. First Edition.

[36] Jolliffe IT, Cadima J. Principal component analysis: A review and recent developments. Philos Trans Royal Soc A: Math Phys Eng Sci 2016;374(2065):20150202. https://doi.org/10.1098/rsta.2015.0202.

[37] Timoshenko S, Goodier JN. Theory of Elasticity. Second Edition. New York, NY: McGraw-Hill; 1951. p. 438–52.